ALTAIR performance and updates at Gemini North

Julian C. Christou[a*], Benoit Neichel[b], François Rigaut[b], Michael Sheehan[a],
Richard M. McDermid[a], Gelys Trancho[b], Chadwick Trujillo[a] & Brian Walls[a]

[a] Gemini Observatory, Northern Operations Center, 670 N. A'ohoku Place, Hilo, HI, USA 96720
[b] Gemini Observatory, Southern Operations Center, c/o AURA, Casilla 603, La Serena, Chile

ABSTRACT

We present up-to-date performance characteristics for natural guide star (NGS) operation of the ALTAIR adaptive optics system at the Gemini N. 8m telescope. These results are obtained from a nightly performance monitoring campaign where we obtain a consistent set of point spread functions (PSFs) over a broad range of observing conditions. These results are compared with system modelling and circular buffer information from the Altair adaptive optics (AO) system. The latter show residual tip-tilt errors with a median rms ~ 18.5 mas. We also present preliminary results from a new operational mode of the laser guide star (LGS) AO which will eventually yield all-sky access with image FWHM ~ 0.1" – 0.2".

Keywords: Adaptive Optics, Natural Guide Star, Laser Guide Star, Performance, Strehl Ratio.

1. INTRODUCTION

Altair is the facility AO instrument at the Gemini North 8m telescope situated on the 4200m summit of Mauna Kea in Hawai'i. The instruments was first commissioned as an NGS system in 2003 [1] and upgraded to an LGS system in 2007 [2]. It is a highly requested instrument for the Gemini science community and is scheduled nightly for NGS operation and from 4-16 days/month for LGS operation. As a facility instrument, it is designed to feed an AO corrected beam into the science instrumentation. The current instrument suite consists (a) the **N**ear-**I**nfra**R**ed **I**mager and Spectrometer, NIRI, which provides a range of imaging and spectroscopy options in the 1-5 micron wavelength region and (b) the **N**ear-Infrared **I**ntegral **F**ield **S**pectrometer, NIFS, which provides 3D imaging spectroscopy. Shortly it will also be used in conjunction with a refurbished **G**emini **N**ear-**I**nfra**R**ed **S**pectrograph, GNIRS, which will offer a wide variety of spectroscopic capabilities when it is commissioned later in 2010.

It has been noted that Altair appears to underperform yielding lower Strehl ratios than expected and in order to understand these performance limitations, we have instigated a regular, almost nightly, monitoring program using the Altair tuning star during evening twilight. This enables a self-consistent set of measurements, focal-plane imaging using NIRI and closed-loop circular-buffer (CB) data, to analyse the performance over a broad range of observing conditions. These data are compared with modelling of the system's performance.

In addition, we have been upgrading the LGS system with modifications to the **S**low **FO**cus sensor (SFO) and to the tip-tilt (TT) guide star system – STRAP. A new LGS operating mode has been investigated and we present initial results showing how a TT guide star ~ 6' from the science target can be used to increase the applicability of LGS eventually to almost all-sky coverage. This test mode makes use of one of the telescope's peripheral wavefront sensors for TT sensing and M2 correction in place of the internal STRAP unit and TT mirror.

2. MEASURING AND MODELLING ALTAIR NGS PERFORMANCE

As mentioned above, we have instigated a regular AO monitoring program which obtains both focal-plane imaging and Altair NGS circular buffer during the beginning of each night's operations during twilight. The AO system is operating at 1 frame rate of 1 KHz. The focal plane measurements are obtained using NIRI and we have converged on a program of 16 images each in H (1.65 μm) and K' (2.12 μm) bands. Each image has an exposure time of t_{exp} = 0.051s, the shortest possible in regular operation, which is chosen to minimize the effect of residual TT errors. The 16 frames are obtained in a 4 × 4 dither pattern for improved background subtraction, necessary for the best Strehl ratio determination. After the image sequence has been obtained the AO loop is opened and the ~ 60 sec of Altair CB data are recorded. Fig. 1 shows sample corresponding *K*-band (top) and *H*-band (bottom) images under a range of seeing conditions. Each image is the shift-and-add (SAA) PSF, using sub-pixel peak-shifting, at that wavelength for a particular night.

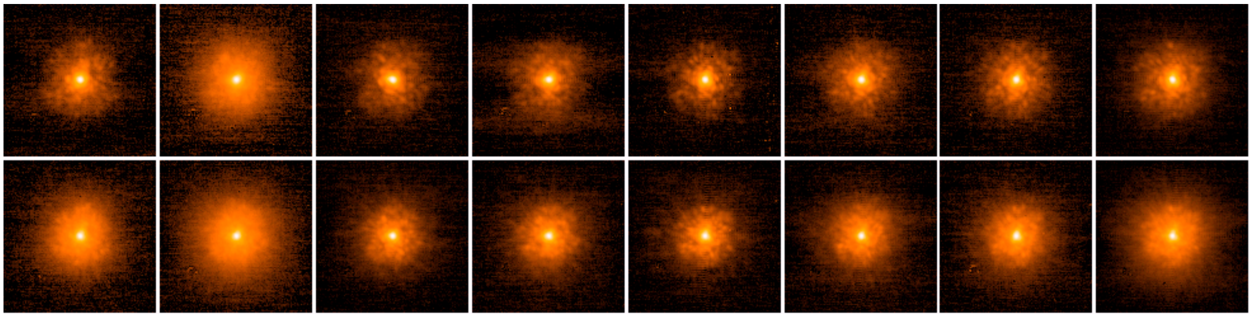

Fig. 1: Corresponding K-band (top) and H-band (bottom) averaged PSFs for different nights (logarithmic display).

2.1 Image Metrics

Each of the PSFs is characterized by three different metrics. These are the Strehl ratio (*S*), the full width at half-maximum (FWHM) and the 50% encircled energy width also known as the full width at half power (FWHP). Strehl ratio is commonly used as a measure of AO system performance and is defined as the relative peak heights of the corrected image to an ideal image through the same optical system and therefore $S < 1$. Its computation is problematic with measured images at the best of times and for the results presented here we have applied a consistent technique. Its measured value is affected by the image pixelation, which includes binning due to the finite pixel size, and by normalization of the total power within the ideal and measured images. The binning is taken into account by modelling the ideal PSF on a greatly oversampled grid which is then binned down to the NIRI image scale of 0.022"/pixel. The binned PSF has a Strehl ratio ~ 93% of the unbinned PSF. The sub-pixel peak values of the measured images were obtained from Fourier interpolation. The ideal and measured images were normalized within a radius of ~0.8" depending upon the signal-to-noise (SNR) ratio of the delivered images. The FWHM is dependent upon the peak value determination and is measured by interpolating the pixel values of the peak-shifted image. Comparison with FWHM measurements of Fourier interpolated images indicate that the pixelated FWHM values are accurate to within 10%. The measurement is actually obtained from the azimuthally averaged radial profile of the PSF and does not take into account asymmetries of the PSF core. The 50% encircled energy is computed by integrating the azimuthally averaged radial profile from the peak out to the SNR-limit and interpolating the radius for the half-power value. Seeing estimates are automatically recorded in the image headers from the Altair diagnostics. The seeing is computed from the r_0 estimates determined from the wavefront sensor such that $\theta = \lambda / r_0(\lambda)$ where $\lambda = 0.5\mu$m.

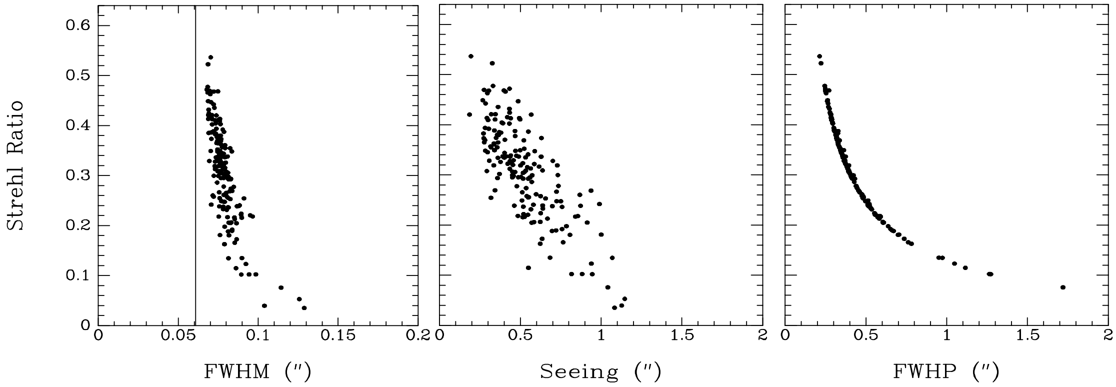

Fig. 2: *K*-band image metric measurements showing variation of the Strehl ratio with image FWHM, Seeing and 50% encircled energy. The solid line in the FWHM represents that for an ideal diffraction-limited image.

Fig. 2 compares the *K*-band metrics as measured from the nightly average tuning-star PSF. As can be seen the data have been accumulated over a broad range in seeing conditions from the excellent super-seeing at ~ 0.2" to the very poor cases at > 1". There is a clear trend that as the Strehl ratio increases the Seeing decreases with the highest Strehl ratios are ~ 52%. There is, however, significant scatter in the Strehl Ratio - Seeing plot. The FWHM estimates indicate a small dispersion is resolution as the Strehl ratio decreases to 10%. The Strehl ratio – FWHP plot shows a very strong inverse quadratic correlation. The *H*-band metrics (fig. 3) show similar distributions but with lower Strehl ratios, having only a 30% maximum, and smaller FWHM but being a larger fraction of the corresponding fully-diffraction-limited image. The ratio of *K*-band to *H*-band Strehl ratios ~ 2× as seen in fig. 4 which plots the corresponding nightly averaged Strehl ratios for the two imaging bands.

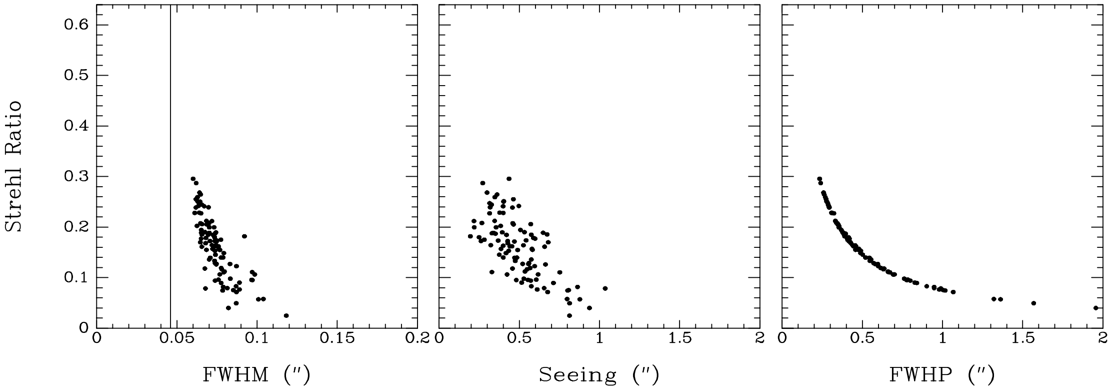

Fig. 3: *H*-band image metric measurements showing variation of the Strehl ratio with image FWHM, Seeing and 50% encircled energy. The solid line in the FWHM represents that for an ideal diffraction-limited image.

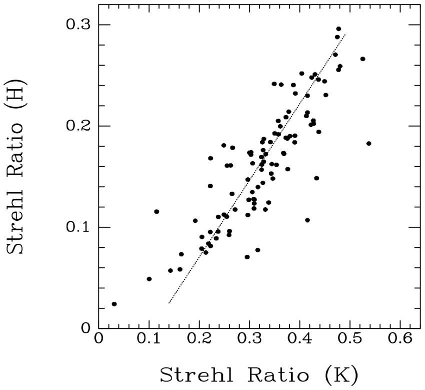

Fig. 4: Comparison of the nightly-averaged *K*-band and *H*-band Strehl ratios. The *H*:*K* band ratio is ~ 0.75 as indicated by the dotted line.

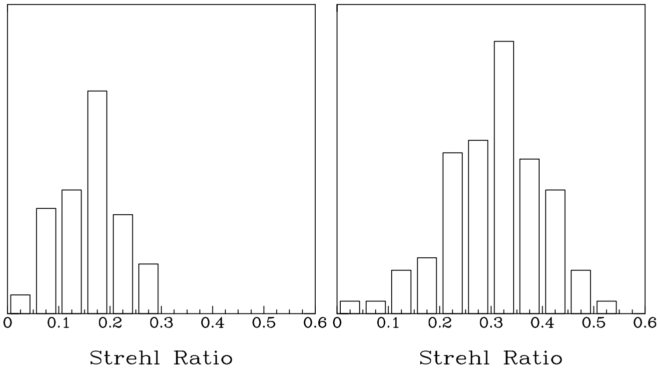

Fig. 5: Strehl ratio histograms for the *H*-band (left) and *K*-band (right) focal plane data.

2.2 Data Binning

The large scatter in the *H*-band and *K*-band image metrics with the seeing, as shown in the previous sub-section, makes it difficult to evaluate and predict the system's performance. In order to reduce this effect, the metric data was binned according to the measured Strehl ratios. Fig. 5 shows the Strehl ratio histograms for both imaging bands with Strehl ratio bin sizes of 0.05. Average PSFs were computed for each Strehl ratio bins for each data set. These are shown in figs. 6 and 7. These selected PSFs clearly show the degradation in image quality with Strehl ratio. Note that for both imaging bands, there is a static residual speckle pattern clearly visible in the high Strehl ratio case which is slowly lost in the residual seeing halo as the compensation degrades. The persistence of this speckle pattern indicates this is Altair related, i.e. after the AO fold in the Gemini optical path, as the focal plane data is not taken at any fixed Cassegrain rotator position which would rotationally blur out any residuals from in front of the AO fold. It is visible in both bands and is high-order and could well be in a non-common path aberration not able to be corrected by the high-resolution wavefront sensor (HRWF) which measures the beam in the science path downstream of Altair.

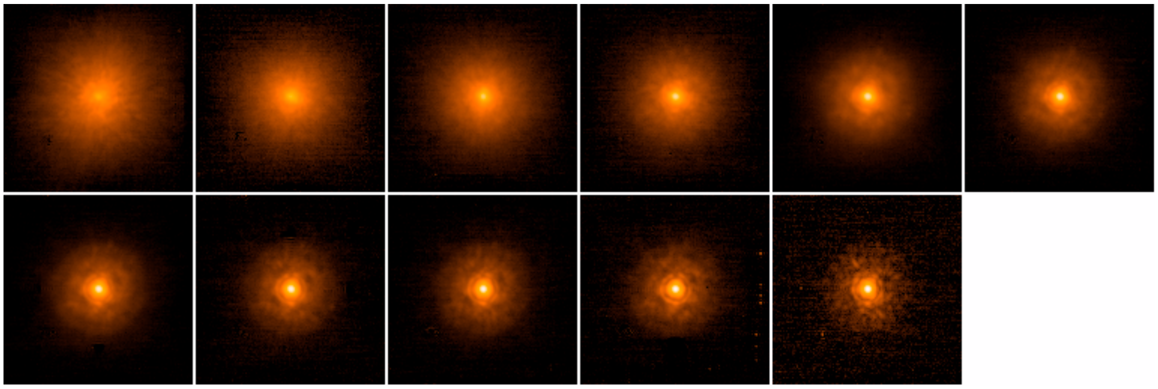

Fig. 6: Strehl ratio binned average PSFs for the *K*-band data. The bins correspond to those is the histogram in Fig. 5.

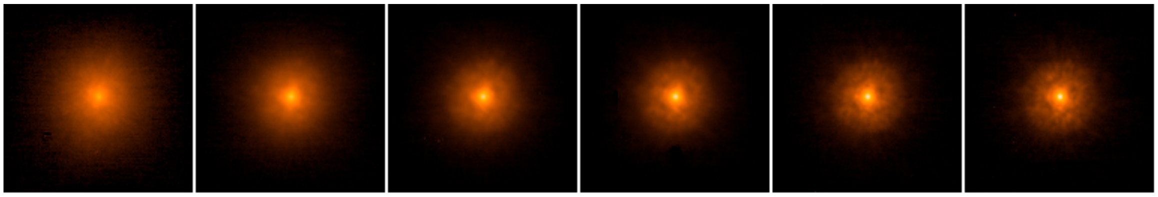

Fig. 7: Strehl ratio binned average PSFs for the *H*-band data. The bins correspond to those is the histogram in Fig. 5.

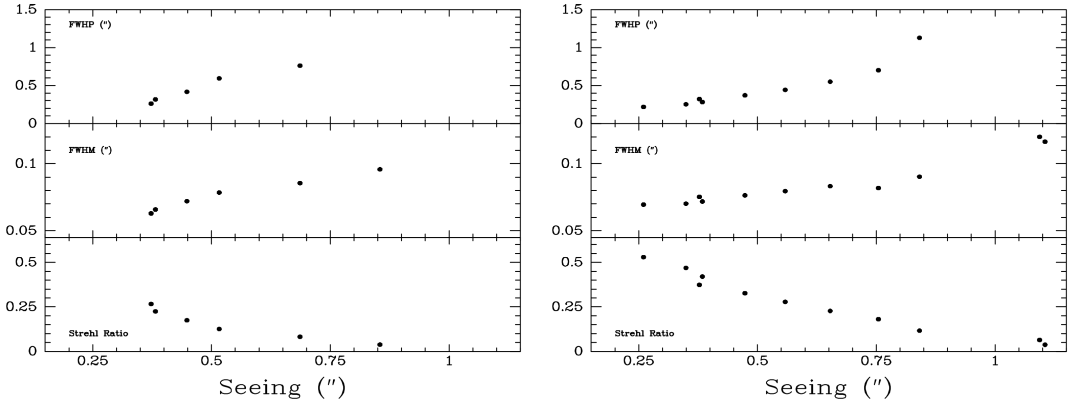

Fig. 8: *H*-band (left) and *K*-band (right) image metrics (bottom-to-top: Strehl ratio, FWHM, FWHP) as a measure of the seeing.

From these binned images we are able to investigate the AO performance as a function of the seeing. Fig. 8 illustrates this by plotting the three metrics for both the binned *H*-band and *K*-band data sets. Clear trends are visible illustrating the expected improvement in performance in all three metrics as the seeing increases.

2.3 Residual Image Motion

Recalling the large scatter in the Strehl ratio – Seeing plots in figs. 2 & 3, the obvious question to conside is why there is such a scatter. The Strehl ratio precision is to within 0.05 and the wavefront sensor seeing estimates are considered to be reliable to 0.1″ which lies within the apparent scatter of both data sets. In order to better understand this scatter it is informative to look at the raw image plane data. *H*-band and *K*-band data from two consecutive nights are shown in figs. 9a and 9b respectively.

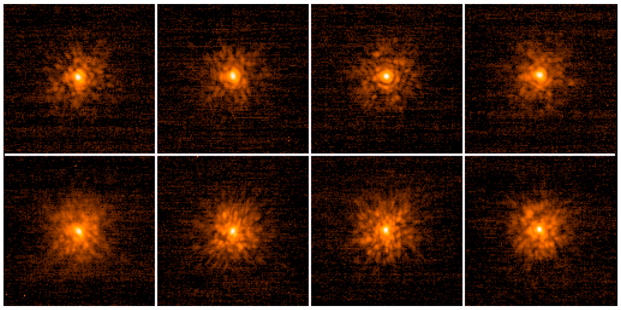

Fig.9a: Four sequential *K*-band frames (top) and *H*-band frames (bottom) obtained on UT 20090807 (logarithmic display).

$$\langle S_K \rangle = 0.47 \text{ and } \langle S_H \rangle = 0.34$$
$$\langle \theta \rangle = 0.30''$$

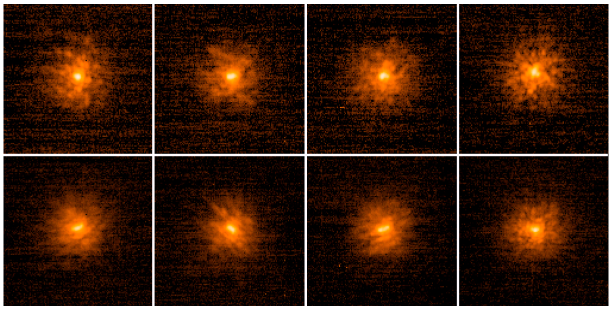

Fig.9b: Four sequential *K*-band frames (top) and *H*-band frames (bottom) obtained on UT 20090806 (logarithmic display).

$$\langle S_K \rangle = 0.22 \text{ and } \langle S_H \rangle = 0.14$$
$$\langle \theta \rangle = 0.52''$$

Investigation of the image cores for these data show the high Strehl ratio to have compact symetric cores whereas the lower Strehl ratio data have very elongated or smeared cores showing a definite orientation. This is more clearly seen in the *H*-band images where the diffraction-spot is smaller and the elongation is ~ 3:1. Compare with the *H*-band image cores in fig. 9a. This illustrates a residial tip-tilt (TT) problem. To investigate this further, we looked at the Altair closed-loop telemetry data and the residual global TT in particular. Statistical analysis of the residual TT show significant image motion. The median value of over 100 measurements has an RMS TT (root sum square of the tip and tilt vales) of 18.4 mas with a range of values from 12.7 mas – 68.3 mas although most are < 30 mas as can be seen in the histogram in fig. 10. Assuming that these dispersions are Gaussian in nature then the FWHM (2.3548σ) ~ 44 mas which would add significantly to the size of the diffraction spot increasing the *K*-band fully diffraction-limited from 61 mas to 75 mas and reducing the Strehl ratios correspondingly to ~ 65%. Thus, this residual image motion would have a significant impact on the measured PSF metrics.

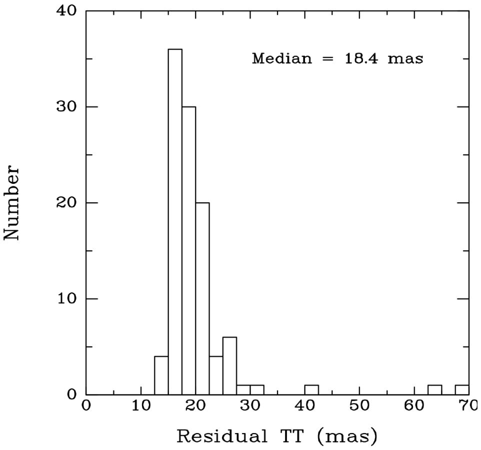

Fig. 10: Histogram of the residual TT as measured from the Altair closed-loop circular buffer data.

2.4 Altair PSF Modelling

The results presented above indicate that there is significant residual image motion affecting Altair performance. In this we present a more detailed modeling of the Altair system using YAO adaptive optics simulation code developed by François Rigaut[1]. The simulations modelled the NGS tuning star observing conditions as closely as possible for a wide range of D/r_0 with $0.2'' < \theta < 1.4''$. YAO produces a PSF for each set-up and these were then measured the same way as the NIRI PSFs. The affect of residual image motion was modelled by convolving the PSFs with circularly symmetric Gaussians with $\sigma = 10$, 15, 20 and 25 mas. The results of these simulations are shown in fig. 11 which compares the YAO models to the nightly averages shown in figs. 2 & 3. The 0 mas residual image motion case compares very well with the data given the uncertainties in the seeing estimates. For the Strehl ratio vs. Seeing plots it nicely represents an upper limit on the Altair compensation for both imaging bands. It is interesting to note that the measured Strehl ratios, especially for the better seeing cases, would appear to be more clumped between the 15mas – 20 mas residual blurring contours. The measured data do not agree as well for the poorer seeing cases ($\theta > 1''$) but there are systematic measurement problems here in terms of Strehl ratio normalisation and undersetimation of the seeing from the WFS data.

---

[1] http://www.maumae.net/yao/

The residual blurring contours also serve to define the diffraction-limited performance, as measured by the FWHM, with the 0 mas contour again representing the envelope of the best compensation.

A significant difference between the models and the data is that the former assumes uniform seeing whereas the measurements indicate that for the most part the quasi-instantaneous seeing is more variable than the model. It should also be noted that the modelling does not take into account non-common path errors in the science leg of the optical system, i.e. from the Altair dichroic to the science fold and to the instrument. These are minimised as much as possible by using the high-resolution wavefront sensor (HRWFS) on the Altair internal calibration source.

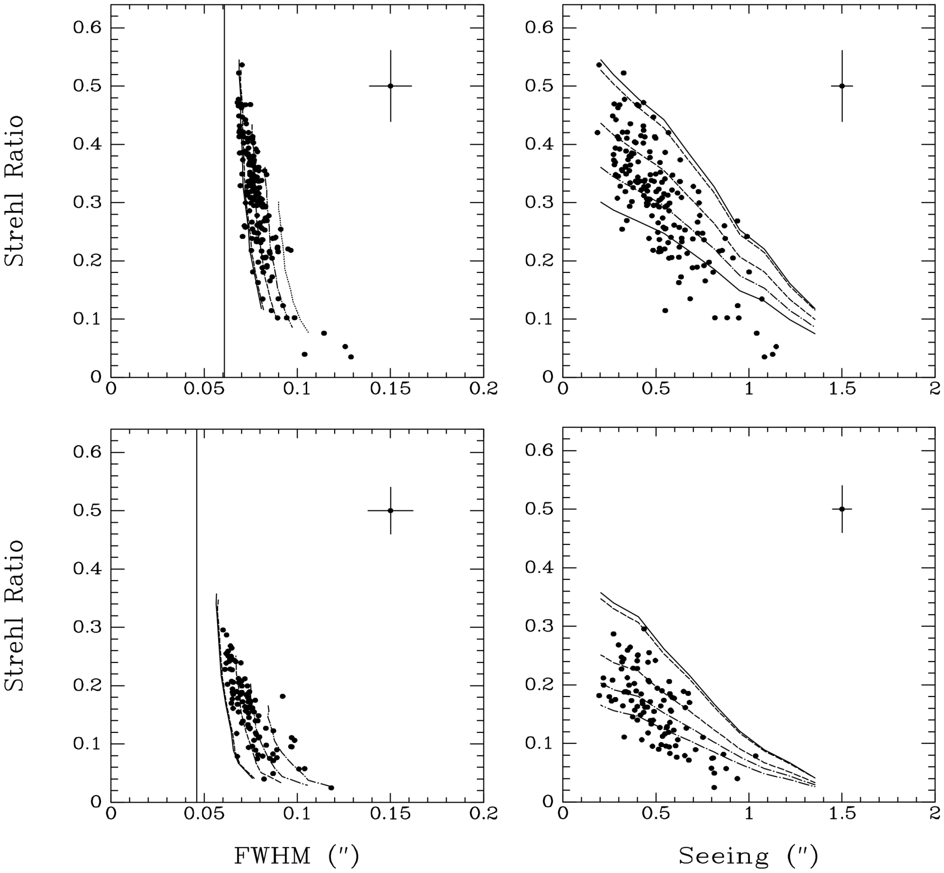

Fig. 11: K-band (top) and H-band (bottom) PSF metrics for the nightly tuning star averages compared with the YAO simulations for 5 different residual image motion cases, 0. 10, 15. 20 and 25 mas. The error bars on each plot represent the mean nightly dispersions over the complete data set.

2.5 Circular Buffer Frequency Analysis

The CB data demonstrates that there is significant residual TT error within the closed-loop operation. The question is what are the causes and can they be mitigated?

We have looked at the avearged power spectral distributions (PSDs) of the residual TT for the two axes and these are shown in fig. 12 for the on-sky data (top) and the internal calibration source (bottom). The on sky PSDs shows a number of noticeable features. The first is the very low-frequency term at ~0.4 Hz which is most likely environmental such as wind induced vibration on the secondary mirror M2 and its support structure as. The second feature, also only visible in the on-sky data, at 10 Hz $< f <$ 20 Hz corresponds to local telescope dynamics such as tracking and guiding. There is also a “forest” of significant power from 40 Hz $< f <$ 100 Hz visible in both distributions which are most likely the results of vibrations on the instrument support structure (ISS) where Altair and the other instruments are mounted behind the primary mirror M1. The “spikes” at ~120 Hz and ~ 240 Hz are most likely due to the Altair cooling fans as they are multiples of 60 Hz. It is interesting to note that the calibration source PSDs show significant "spikes" at 17 Hz and 127 Hz which are very noticeable in the cumulative PSDs shown in fig. 13. These frequencies, which have been identified as being resonances in the ISS, are present in the on-sky data but substantially smaller. Images of the calibration source using NIRI have shown streaking indicating that the calibration source is resonating at these frequencies. There are no such obvious dominating frequencies in the on-sky data.

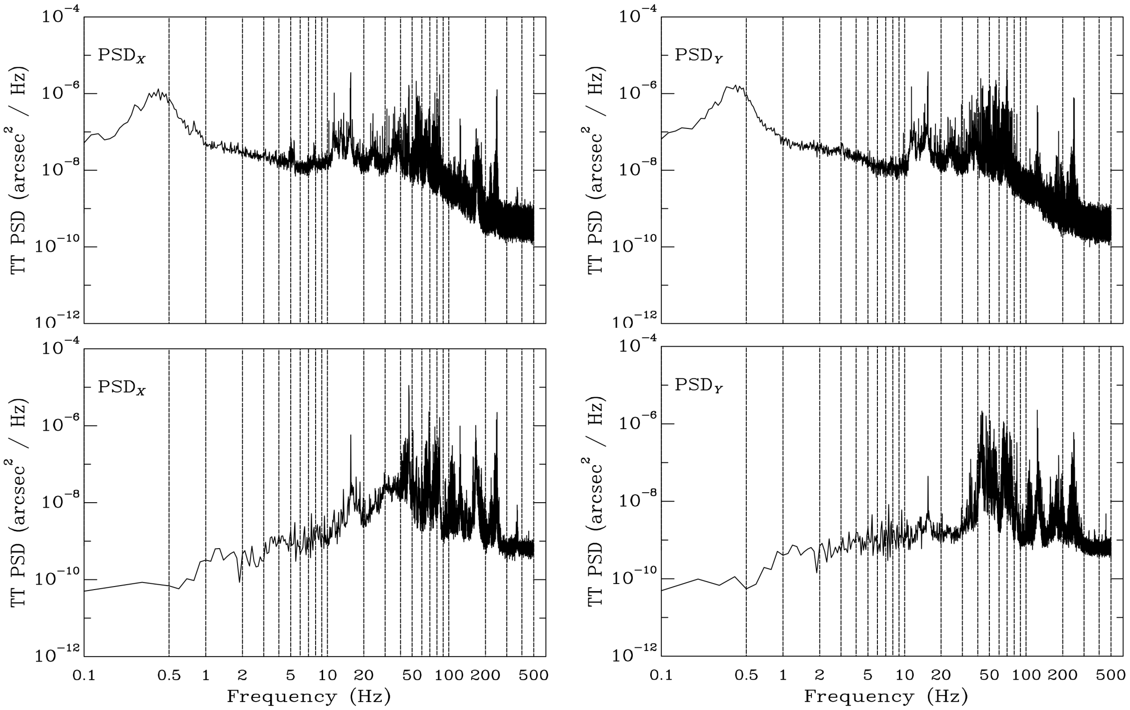

Fig. 12: Averaged power spectral densities for the residual tip-tilt from the nightly Altair tuning star circular buffer data (top) and the daytime internal calibration source (bottom).

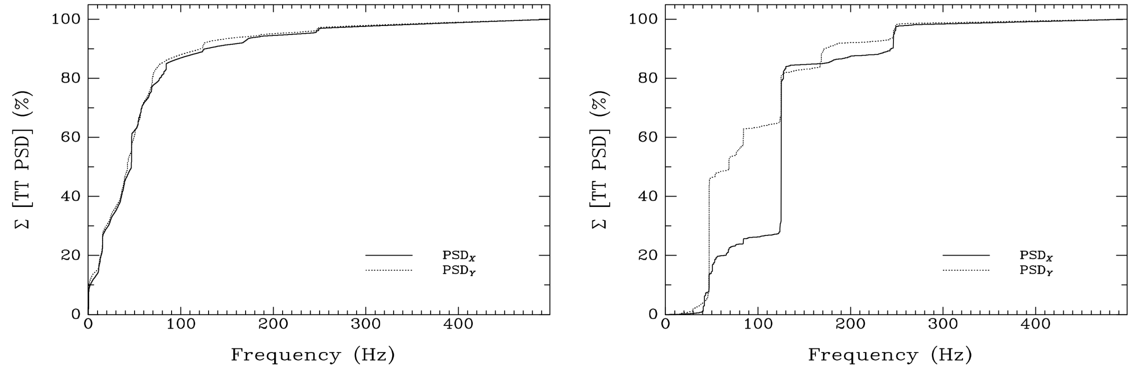

Fig. 13: Averaged cumulative power spectral densities for the residual tip-tilt from the nightly Altair tuning star circular buffer data (left) and the daytime internal calibration source (right).

The focal plane images have an exposure time of 0.051secs and therefore sample all frequencies > 20 Hz. Thus ~ 70% of the total residual TT power is sampled so that the median residual TT is reduced from ~18.5 mas to ~15.5 mas. This remaining TT power comes from the 40 Hz < f < 100 Hz "forest".

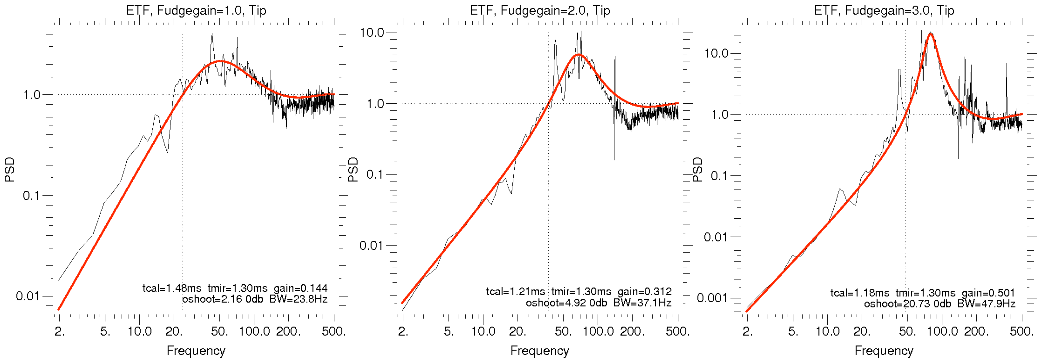

Fig. 14: TT error transfer functions using the Altair internal calibration source for three different "typical" gain settings. The solid red lines are model fits through the data.

The contribution of the different frequencies to the residual TT is determined by the TT error transfer function (ETF) which is simply the ratio of the closed-loop TT PSD to the open-loop TT PSD as measured on white noise. Altair uses a dynamic sub-aperture centroid offset measurements which reflects the size of the image on each of the quad cells. On top of that, the TT loop gain is adjusted based on a modal optimization.

In order to estimate the ETF we ran Altair using the calibration source with the dynamic gains turned off and with three separated fixed gain cases. Results for both tip and tilt are similar and those for the tip mode are shown in fig. 14. The TT bandwidth is estimated to be around 40Hz, and the overshoot lies in the frequency domain 40Hz to 100Hz. Unfortunately, this is the frequency range where there is the most significant contribution according to the TT PSDs. In The data were fit with a simple model consistent with a two frame delay loop, with a TTM lag around 1.3msec which is in good agreement with the constructor data.

2.6 Further Work

A thorough understanding of the sources of error in both NGS and LGS operation is required. It is important to note that Altair/NGS performance is actually very good within the instrument itself. Using the internal Altair calibration source with NGS closed-loop operation, we obtained short exposure NIRI images ($t_{\rm exp}$ = 51 msec) with Strehl ratios up to 90% at *K'*. Unfortunately this wasn't always consistent and investigation of the individual images showed streaking of the PSF consistent with the residual TT frequencies shown for the calibration source PSDs in figs. 12 & 13, and indicating that the calibration source is not mechanically stable. This stability will be investigated and addressed during upcoming shutdowns.

The findings from the NGS PSF campaign, presented above, reveal that significant residual TT errors (median value ~ 18—20 mas) which affect the on-sky performance. In order to thoroughly mitigate these, we need to understand their sources. Some are external to the science leg such as the environmental mode ($f < 1$ Hz) and the telescope dynamic mode (10 Hz $< f <$ 20 Hz). The most significant contribution lies in the 40 Hz $< f <$ 100 Hz range and is common to closed-loop operation with the Altair calibration source and also on-sky. This is the region where there are resonances of the instrument support structure and on some of the Altair relay optics. The most likely source of these resonances, and the instrument response to them, are the cold-heads on the various instruments. A thorough mechanical/vibrational analysis is planned during telescope shutdown to work towards identifying and eventually reducing these.

Analysis of the NGS/TT error transfer function shows that, over this frequency range, it is actually amplified further reducing the AO performance. Increasing the gain would increase this overshoot in the ETF. Altair has a dynamic gain adjusting to the observing conditions and the ETF suggests that when those conditions require a higher gain then there will be increased TT error. If this is not possible to reduce the vibrations at the source, then the implementation of a woofer-tweeter [3] or Kalman filter scheme [4] would improve the rejection at low frequencies and to translate the overshoot toward higher frequencies, where the TT contribution is less critical.

We have also measured the ETF of the STRAP loop for LGS operation following the same procedure as for the NGS TT loop. These preliminary measurements found bandwidths consistently smaller than for NGS TT (~25Hz compared with the expected ~40Hz). Further studies are needed to characterize and understand what is actually happening here and how and if these tie into the telescope/ISS vibrations.

Even with minimization of the TT errors, there is a further error source which fundamentally limits the AO performance. This is the print-through of the six M2 attachment points and the resulting phase map is shown in fig. 15 and the rms phase error ~ 20—30nm.

Altair is mounted at Cassegrain behind the rotator so that fixed pattern on the M1/M2 beam will rotate onto the Altair pupil. These are high-order aberrations which alias into lower spatial frequencies correcting for aberrations which are not present thus not only introducing a high-order aberration but also a low-order term due to the aliasing. These can be corrected for observations requiring a fixed Cassegrain rotator position. Unfortunately, most observations are taken with the Cassegrain rotator on, ~ 95% of all Altair observations. (Note that all observations presented in this paper were obtained at different Cassegrain rotation angles.) Future work will investigate and characterize the effect of this print through.

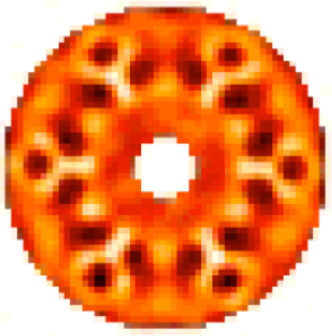

Fig. 15: M2 print-through phase map.

In addition to the work presented here, we have also recently instigated a program for PSF reconstruction from the Altair CB data [5,6] for which a thorough understanding of the error sources is necessary.

3. ALTAIR LASER GUIDE STAR UPGRADES

During the last year there have been a number of upgrades to the LGS operation of the AO system. Unlike the NGS mode of operation, LGS operation uses the sodium laser for the high-order correction and a natural guide star for both TT and focus correction, the latter because of the changes in the altitude of the sodium guide star due to density fluctuations in the sodium layer. In addition, we have also initialised a new mode of operation which will increase the sky coverage of LGS AO by using a peripheral wavefront sensor to drive the TT and focus correction. This allows for a TT/focus star further off-axis with the drawback that the corrections will be not be diffraction-limited.

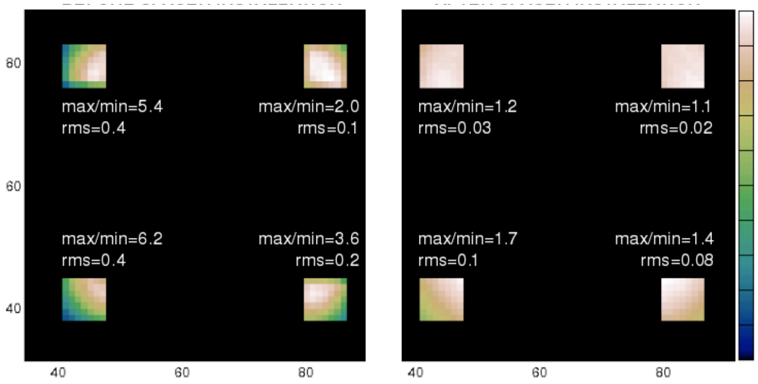

Fig. 16: Illumination pattern on the SFO sub-apertures before (left) and after (right) the spacer installation to shift the SFO by 49 mm.

3.1 SFO and STRAP Upgrades

Both the natural guide star Slow Focus Sensor (SFO) and the TT sensor (STRAP) have been planned for upgrades. The new STRAP avalanche photo diode (APD) quad cell was tested in December 2009 and was found to have a bad quadrant, i.e. one with ~15% of the quantum efficiency of the other three. The old STRAP has been replaced while the new one has been returned to the manufacturer for replacement.

The SFO is a CCD wavefront sensor which has four subapertures used to measure the focus of the NGS. The subaperture images showed significant vignetting and a close inspection of the unit shows that it was ~ 50 mm from the pupil conjugate. This was corrected by installing a spacer and the changes can be seen in fig. 16 where the response to uniform illumination (sky) across SFO has been substantially reduced and is much closer to unity. In addition to the hardware upgrades, we have also modified the SFO centroiding algorithm. The first was to redefine the centroid box sizes and locations to make them fully compatible with 1 × 1 and 2 × 2 binning and to accommodate both the NIRI and NIFS focus offsets. The second modification was to improve the thresholding. In the original code, the thresholding was set relative to the peak value in each subaperture. It is now computed relative to a mean background b and noise σ_b in each subaperture. Both are computed using pixel values in a guard-band" of 2 pixel width around the edge of the window and is done iteratively in order to exclude "bad" pixels. The threshold is simply $b + n\sigma_b$ where the default value of n is 3.5 but can be modified. The SFO uses visible light and in some cases the guide star is embedded in nebulosity. In adds a significant background to each subaperture window and because of the non-uniformity (see fig. 16) can lead to biases in the computed centroids. This can be mitigated by using a more sophisticated background subtraction algorithm estimating the mean value of each side of the window and from these estimating and then subtracting a tilted plane. Fig. 17 illustrates the improved centroid estimate using simulated background images created with actual bright star and sky SFO measurements, the latter being scaled for the different background strength cases. The tilted plane subtraction algorithm will be implemented at the next upgrade cycle.

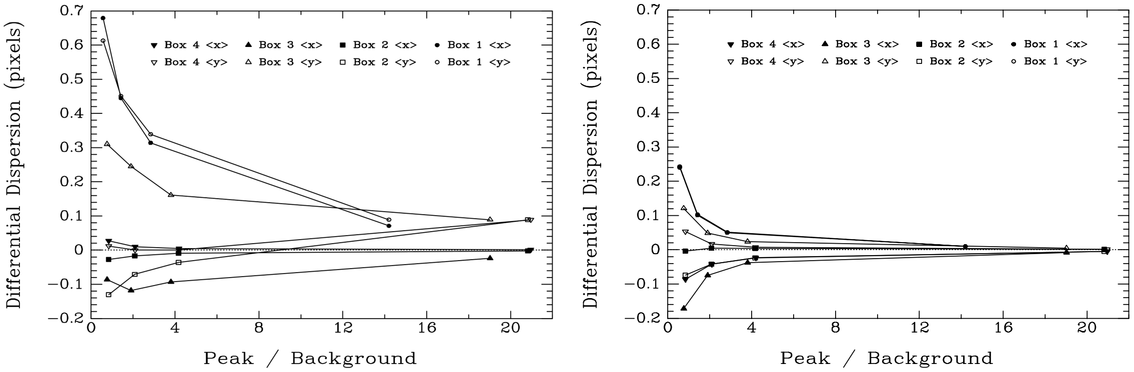

Fig. 17: Bias introduced by the background on the mean centroid locations for the 4 different windowed subapertures using (left) the new background subtraction algorithm and (right) the tilted plane subtraction. The image scale is 90 mas/pixel.

3.2 Laser Guide Star Operation with Peripheral Wavefront Sensing

For existing Altair/LGS operation the TT star has to lie < 25" from the target because of the limiting field-of-view (FoV). This limits the available sky coverage. In order to increase the sky coverage we have tested the use of one of the telescope's peripheral wavefront sensors (PWFS, hereafter referred to as P1) for the TT guide star. This gives access to guide stars at significantly greater separations ~ 6'. Fig. 18 shows the observing tool set-up for recent validation of this observing mode in May 2010. The fig. shows the acquisition field with the Altair/LGS FoV (small square box) at the center. The shaded area represents P1 centered on a bright TT star ~ 6' from the LGS field. The Altair TT guide star has a magnitude limit of V ~ 17 whereas V_{P1}~ 10 so there is a trade off between FoV access and guide star magnitude. This is a similar to the observing mode described by Davies et al. for the VLT [7].

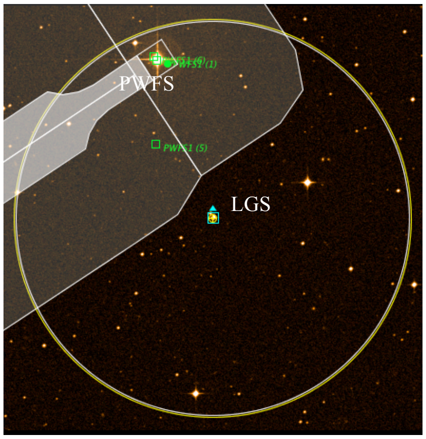

Fig. 18: Observing set-up for LGS+P1 observing.

The validation experiment comprised standard LGS observing using both STRAP and SFO on a bright star with high-resolution NIRI imaging (22 mas/pixel) which provided the "ground truth". This was followed by LGS observing with the SFO and TT loops disabled but with P1 correction of the TT. Contamination by the Rayleigh backscatter of the sodium laser beam affected P1 guiding using the V (450 nm – 700 nm) and R filters (550 nm – 900 nm) so that all guiding was done with the B (300 nm – 500 nm) filter. For each observing mode, a series of ten K-band images (λ = 2.19μm, t_{exp} = 10 secs) were obtained on NIRI. The Altair measured seeing for both was ~ 0.6". The average of these images is shown in fig. 19 along with the azimuthally averaged radial profiles. The Strehl ratio of the standard LGS images is 16.9 ± 1.2 with a FWHM of 90 mas compared with S = 5.8 ± 1.6 and FWHM = 177 for the LGS+P1 configuration. This represents a factor of 3 improvement over the seeing and has a FWHM only twice that of the standard LGS observing mode.

In order to make this a fully supported operation mode there is some future work planned. This involves having the TT/Focus corrections being sent directly from P1 to Altair along with software changes to support rapid switching from one observing mode to the other. In addition there are some hardware changes to be made. The P1 sensitivity can be increased by using the full wavelength range of the WFS and this involves using a notch-filter to remove the Rayleigh beam contamination. Additionally it is also planned to replace the current 6 × 6 lenslet array in P1 with a 2 × 2 array further increasing the sensitivity. The gain in sensitivity will increase the sky coverage as illustrated in fig. 20.

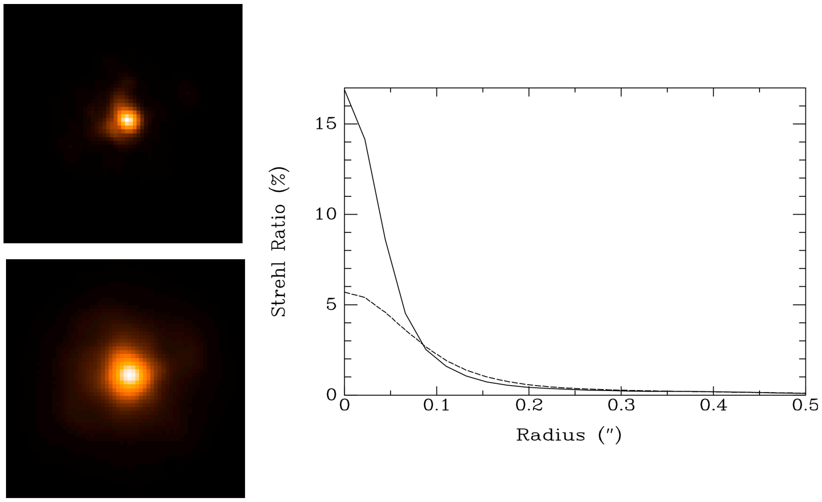

Fig. 19: Averaged PSFs for standard LGS operation (left top) and LGS+P1 (left bottom) and their azimuthally averaged radial profiles (right).

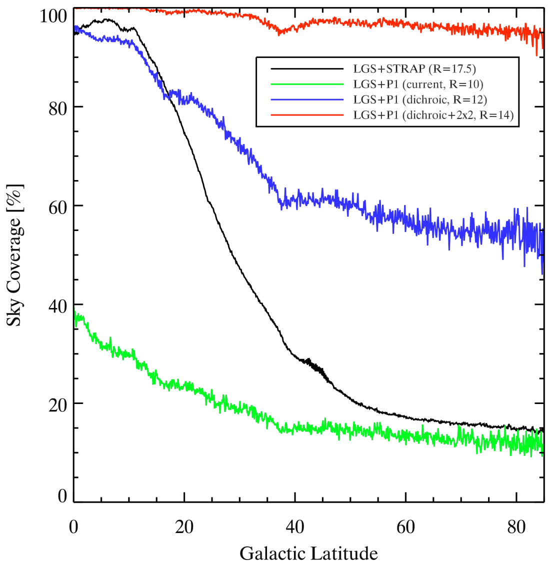

Fig. 20: The benefits of using LGS+P1. The current LGS+STRAP mode is the black line which drops rapidly away from the Galactic Plane. The green line shows the sky-coverage with the existing LGS+P1 magnitude limit, the blue line shows the improvement by using the Na notch filter and the red line with the replacement of the 6 x 6 WFS with a 2 x 2. Note that this will yield almost 100% sky coverage.

For this plot, the entire USNO catalog was used to estimate the stellar density in many small patches all around the sky. This stellar density was then combined with the current LGS+STRAP field to generate the black line and the LGS+P1 lines were generated using an annulus between 4.8' to 6.8' modelling the unvignetted P1 patrol field.

4. SUMMARY

We have presented an analysis of the Altair NGS performance looking at focal plane imaging as well as closed-loop circular buffer data obtained on a regular basis over a variety of seeing conditions. From this we have been able to characterize the Altair NGS performance using a number of metrics, specifically Strehl ratio, FWHM and 50% encircled energy and show that the significant residual tip-tilt signal on the closed-loop correction (median value ~ 18—20 mas) which, when compared with system modelling, accounts for most of the degraded performance. We have identified the critical frequency range for the vibrations which critically contribute to the residual TT and find these to be amplified by the ETF of the NGS TT. For improved Altair performance it is necessary to identify these vibration sources and mitigate them as best as possible.

We have also presented recent upgrades to the Altair LGS system including the initial testing of a new operating mode, using one of the the peripheral wavefront sensors, P1, as a tip-tilt/focus sensor in place of STRAP and SFO. The current operational model is limited to TTF correction over a small field of view, < 25 mas, from the science target. This limits the number of available targets at Galactic latitudes > 20°. We have demonstrated that under median seeing conditions (0.6") a P1 TT star yields a PSF with a FWHM < 0.2" (twice that of standard operation) and this is well matched to the spatial sampling of NIFS (0.1") [8]. Before this can be made available as a supported operational mode there are some necessary hardware and software changes.

Acknowledgements

The authors would like to thank the many of the Gemini Observatory Science and Engineering staff for the assistance with data collection and for many useful discussions concerning the AO/telescope system, in particular Dolores Coulsen, John White, Mathieu Bec, Maxime Boccas, and Markus Hartung. In addition we'd also like to thank Jean-Pierre Véran and Laurent Jolissaint for many fruitful discussions.

The Gemini Observatory is operated by the Association of Universities for Research in Astronomy, Inc., under a cooperative agreement with the NSF on behalf of the Gemini partnership: the National Science Foundation (United States), the Science and Technology Facilities Council (United Kingdom), the National Research Council (Canada), CONICYT (Chile), the Australian Research Council (Australia), Ministério da Ciência e Tecnologia (Brazil), and Ministerio de Ciencia, Tecnología e Innovación Productiva (Argentina).

REFERENCES

[1] J.A. Stoesz et al., "Evaluation of the on-sky performance of Altair", Proc. SPIE, 5490, 67—78 (2004).
[2] M. Boccas et al., "Laser Guide Star upgrade of Altair at Gemini North", Proc. SPIE, 6272-3L (2006).
[3] J.-P. Véran et al., "Improved Tip-Tilt Correction with Altair, The Gemini North AO System", ESO Conference and Workshop Proceedings, 56, Ed. D. Bonaccini, p.701 (1999).
[4] C. Petit C., et al., "First laboratory validation of vibration filtering with LQG control law for adaptive optics" Opt. Express, 16, 87-97, (2008)
[5] L. Jolissaint, J.-P. Véran & J. Marino, "OPERA, an automatic PSF reconstruction software for Shack-Hartmann SO systems: application to Altair", Proc. SPIE, 5490, 151—163 (2004).
[6] L. Jolissaint et al., "Point-spread function reconstruction for Altair, Gemini North adaptive optics system: first on-sky results", Proc. SPIE 7736-50, (2010).
[7] R. Davies et al., "Laser Guide Star Adaptive Optics without Tip-Tilt", ESO Messenger, 131, (2008).
[8] R. M. McDermid et al., "Weighing black holes using open-loop focus corrections for LGS-AO observations of galaxy nuclei at Gemini Observatory", Proc. SPIE 7736-223, (2010).